ARTICLE

Multiscale Confinement Engineering for Boosting Overall Water Splitting by One-Step Stringing of a Single Atom and a Janus Nanoparticle within a Carbon Nanotube

Quan Quan, Yuxuan Zhang, Shaohai Li,* SenPo Yip, Wei Wang, Pengshan Xie, Dong Chen, Weijun Wang, Di Yin, Yezhan Li, Bilu Liu, and Johnny C. Ho*

Read Online

ACCESS | Metrics & More | Article Recommendations | Supporting Information

ABSTRACT: Enzyme-mimicking confined catalysis has attracted great interest in heterogeneous catalytic systems that can regulate the geometric or electronic structure of the active site and improve its performance. Herein, a liquid-assisted chemical vapor deposition (LCVD) strategy is proposed to simultaneously confine the single-atom Ru sites onto sidewalls and Janus Ni/NiO nanoparticles (NPs) at the apical nanocavities to thoroughly energize the N-doped carbon nanotube arrays (denoted as Ni/NiO@Ru-NC). The bifunctional Ni/NiO@Ru-NC electrocatalyst exhibits overpotentials of 88 and 261 mV for hydrogen evolution reaction (HER) and oxygen evolution reaction (OER) at 100 mA cm^{-2} in alkaline solution, respectively, all ranking the top tier among the carbon-supported metal-based electrocatalysts. Moreover, once integrated into an anion-exchange membrane water electrolysis (AEMWE) system, Ni/NiO@Ru-NC can act as an efficient and robust bifunctional electrocatalyst to operate stably for 50 h under 500 mA cm^{-2}. Theoretical calculations and experimental exploration demonstrate that the confinement of Ru single atoms and Janus Ni/NiO NPs can regulate the electron distribution with strong orbital couplings to activate the NC nanotube from sidewall to top, thus boosting overall water splitting.

KEYWORDS: confinement, single atom, Janus nanoparticle, carbon nanotube, overall water splitting
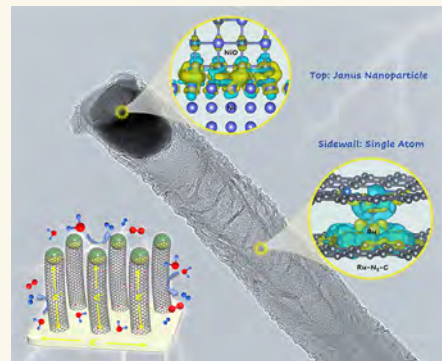
The electrochemical conversion of water into green hydrogen as a clean and renewable fuel has attracted significant attention to relieve the environmental and energy crisis in the future.[1,2] In principle, water electrolysis involves two half-reactions: the cathodic two-electron hydrogen evolution reaction (HER) and the anodic four-electron oxygen evolution reaction (OER).[3−5] However, developing bifunctional electrocatalysts for HER and OER with good performance and stability simultaneously at large current density is challenging, which is paramount for bringing the water-splitting technique to reality.

Confinement of active species at controllable dimensions into diverse porous hosts (i.e., carbons, polymers, and zeolites) has been widely recognized in various catalytic applications for high performance and structural stability. Among them, carbon-confined nanomaterials are highly attractive because the carbon matrix, as a well-conductive support, can effectively stabilize the active species and optimize their local electronic structures.[6−9] Especially, confining metallic nanoparticles (NPs) into nitrogen-

doped carbon (NC) nanotubes has been demonstrated as a general strategy for electrocatalytic water splitting applications under the cladding effect of the robust yet flexible carbon sheath.[10] However, limited active sites in the NC matrix and the poor stability of metal NPs under harsh conditions hinder their practical applications. In this context, atomically dispersed metal sites confined into the NC matrix by coordination with nonmetal atoms have been investigated to improve the accessibility of active species.[11,12] Apart from that, the surface electronic structure modification of metal NPs via constructing a Janus heterostructure can potentially enrich the active sites and improve stability.[13] Therefore, the co-introduction of single-
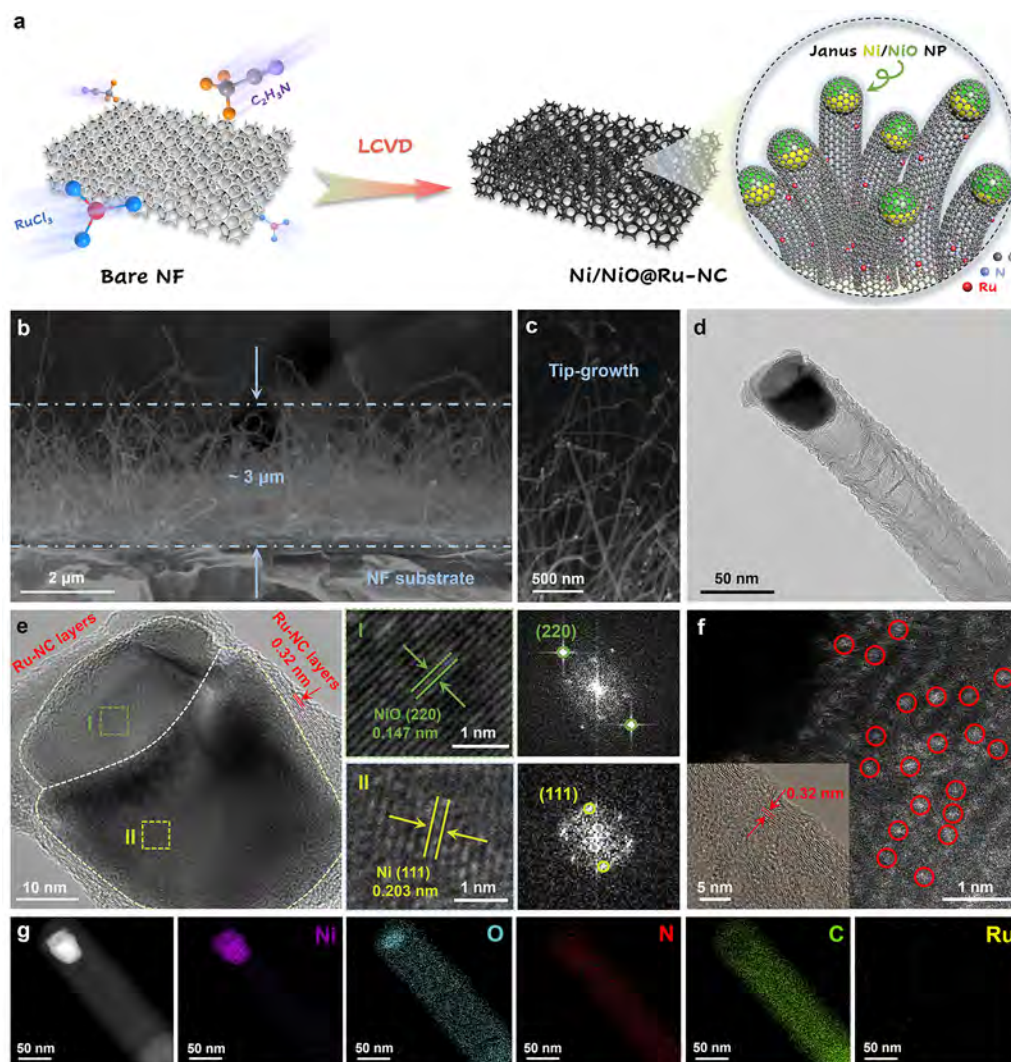
Figure 1. (a) Schematic illustration of the preparation for Ni/NiO@Ru-NC. (b, c) SEM images and (d) TEM image of Ni/NiO@Ru-NC. (e) HRTEM and FFT images of the tip Ni/NiO NP encapsulated by Ru-NC layers. (f) Aberration-corrected STEM image of Ru-NC (inset: HRTEM image of Ru-NC). (g) HAADF-STEM and the elemental mapping images of Ni/NiO@Ru-NC.

atom metal sites in conjunction with Janus metal heterostructures into the NC matrix by the confinement engineering strategy at multiscale is supposed to conquer the existing bottlenecks, thus achieving an impressive catalytic performance.

Herein, as a proof of concept, we develop a one-step liquid-assisted chemical vapor deposition (LCVD) strategy to simultaneously confine Ru atom sites on the sidewalls and Janus Ni/NiO NPs at the apical domains within NC nanotube arrays (denoted as Ni/NiO@Ru-NC). The Ni/NiO@Ru-NC exhibits overpotentials of 88 and 199 mV at -100 and -500 mA cm^{-2} for the HER activity and shows overpotentials of 261 and 318 mV at 100 and 500 mA cm^{-2} for the OER activity, respectively. The Ni/NiO@Ru-NC offers long-term stability (100 h) under harsh reducing/oxidating conditions ($500/-500$ mA cm^{-2}). Additionally, the Ni/NiO@Ru-NC‖Ni/NiO@Ru-NC electrolyzer reaches 100 and 500 mA cm^{-2} at cell voltages of 1.595 and 1.734 V, respectively. Meanwhile, bifunctional Ni/NiO@Ru-NC can stably operate an anion-exchange membrane water electrolysis (AEMWE) system for 50 h under 500 mA cm^{-2} at a voltage of 1.95 ± 0.05 V in 1.0 M KOH at room temperature. As evidenced by density functional theory (DFT) calculations and corresponding experimental results, the

confinement of Ru single atoms and Janus Ni/NiO NPs can effectively regulate the electronic distribution with strong orbital couplings to accelerate electron transportation and enrich active sites through the whole NC nanotube from sidewall to top. The hydrophilic flexible nanotube arrays featuring porous channels can promote mass diffusion and expedite the gaseous product release to strengthen the mechanical stability, refraining from bubble accumulation.

RESULTS AND DISCUSSION

Design and Characterization of Ni/NiO@Ru-NC. The hierarchical Ni/NiO@Ru-NC nanotube arrays are prepared using a one-step LCVD strategy, as schematically illustrated in Figure 1a. Specifically, with the acetonitrile (C_2H_3N) and ruthenium trichloride ($RuCl_3$) bubbled into the high-temperature chamber, a carbothermal reduction process takes place on the pretreated nickel foam (NF) substrate to grow the single-atom Ru anchored N-doped carbon (Ru-NC) nanotube arrays with their apical domains encapsulating Janus Ni/NiO NPs (Figure S1). During this process, C_2H_3N is decomposed into different species, including hydrogen cyanide (HCN) and methane (CH_4), acting as the nitrogenous and carbonaceous
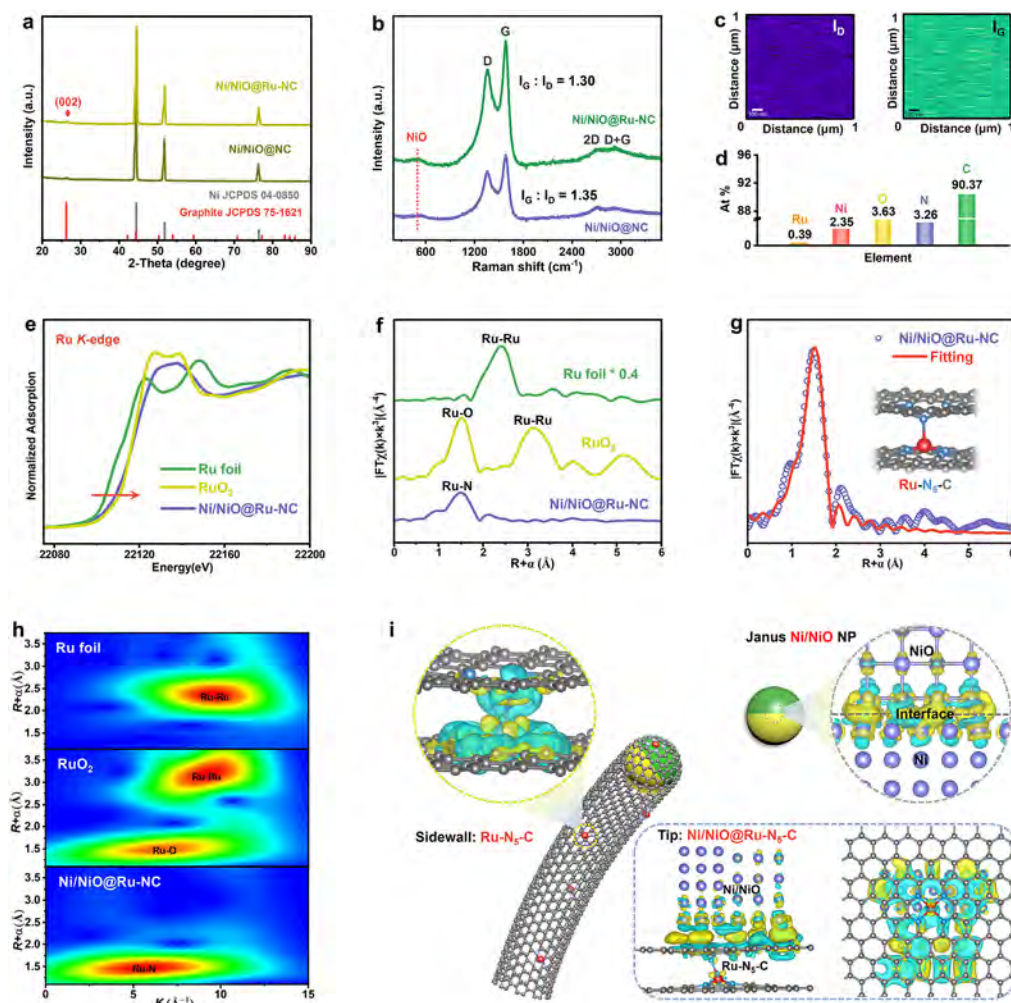
Figure 2. (a) XRD patterns and (b) Raman spectra of Ni/NiO@Ru-NC and Ni/NiO@NC. (c) Raman mapping of D-peak and G-peak intensity and (d) atomic ratio of elements in Ni/NiO@Ru-NC. (e) XANES and (f) FT-EXAFS spectra at the Ru K-edge of Ni/NiO@Ru-NC, Ru foil, and RuO$_2$. (g) FT-EXAFS fitting curve in R space of Ni/NiO@Ru-NC (inset: optimized Ru-N$_5$-C configuration by DFT calculations). (h) WT plots of the k^3-weighted Ru K-edge EXAFS. (i) The differential charge density of Ru-N$_5$-C at the sidewall part, Ni/NiO and Ni/NiO@Ru-N$_5$-C at the top part (yellow contour, electron accumulation; cyan contour, electron depletion).

feedstocks to form Ru-NC.[14] With a NiO layer on the surface of pretreated NF (Figure S2), the Janus Ni/NiO NPs are first exsolved at the beginning. Then, the Ru-NC nanotubes start to grow with the Ni/NiO NPs at the tips, and their length and density increase with the growth time, as revealed by time-dependent control experiments (Figure S3). These observations demonstrate that the Ni/NiO NPs originated from the surface-oxidized NF can catalyze the growth of high-quality Ru-NC nanotubes in an acetonitrile atmosphere by the "tip-growth" mechanism,[15] which is illustrated in Figure S4. The cross-section field-emission scanning electron microscopy (FESEM) images of Ni/NiO@Ru-NC exhibit an array-structure integrated by the aligned, flexible carbon nanotubes on the NF skeleton with a length of *ca.* 3 μm (Figure 1b,c).

As depicted in Figure 1d, a typical transmission electron microscopy (TEM) image of a single nanotube reveals that a Janus Ni/NiO NP is encapsulated at the tip of the Ru-NC nanotube. It can be observed from Figure 1e that, at the tip part, the NP is wrapped by the Ru-NC layers with a lattice fringe of 0.34 nm while a clear heterointerface exists between the two phases within the NP. For the marked I and II regions of the NP part in Figure 1e, the interplanar spacings of 0.147 and 0.203 nm

displayed by high-resolution TEM (HRTEM) image and corresponding fast Fourier transform (FFT) patterns are consistent with the (220) lattice plane of NiO and the (111) lattice plane of metallic Ni, respectively, confirming the coexistence of NiO and Ni phases in the Janus-type NP.[16] Meanwhile, in a typical HRTEM image for the carbon nanotube region (inset, Figure 1f), parallel graphene lattices can be observed with an interplanar spacing of about 0.34 nm, and no obvious Ru clusters or nanoparticles are discerned. Subsequently, scanning TEM (STEM) and the corresponding elemental mapping are applied to evaluate the spatial element distribution in the Ni/NiO@Ru-NC (Figure 1g). It is observed that the Ni element intensively occupies the apical NP region, while the O element concentrates on the top half part of the NP. At the same time, the associated line scans further corroborate the Janus Ni/NiO structure within the tip NP (Figure S5). Moreover, the N and C elements are evenly distributed across the nanotube without the aggregation of the Ru element, indicating the formation of Ru-NC without Ru nanoparticles or clusters formed. In this regard, aberration-corrected scanning transmission electron microscopy (AC-STEM) is carried out to further explore the Ru species' configurations. As presented in

Figure 1f, the brighter spots can be attributed to the isolated Ru sites anchored in the carbon lattice, which are annotated with red circles.[17] The formation of the atomically dispersed Ru can be ascribed to the fact that, during the LCVD-synthesized process, the abundant uncoordinated −CN groups act as Lewis bases to bind Ru complex ions; thus, the Ru site is stabilized and confined in the N-doped carbon matrix as Ru-N$_x$ sites without further Ru assembling.[3]

As a control experiment, the pure C$_2$H$_3$N solution without adding RuCl$_3$ is applied to synthesize the Ni/NiO@NC counterpart under identical conditions. It can be observed from SEM and HRTEM images that there are NC nanotube arrays grown on the NF substrate with the Janus Ni/NiO NPs encapsulated by NC layers on the tip, also following the "tip-growth" mechanism (Figure S6). Therefore, the successful synthesis of Ni/NiO@Ru-NC and Ni/NiO@NC demonstrates the generality and feasibility of the LCVD method to synthesize high-quality carbon nanotubes with Janus NPs and desirable single atoms in one step, which is distinguished from the traditional H$_2$/Ar calcination. Generally, the conventional calcination methods utilize the presynthesized carbonaceous precursors or the CH$_4$/C$_2$H$_4$ gas as carbon sources,[18,19] which require multiple steps to obtain the functional carbon nanotubes.

The X-ray diffraction (XRD) patterns of Ni/NiO@Ru-NC and Ni/NiO@NC display strong diffraction peaks from Ni and NF substrate (JCPDS no. 04-0850) (Figure 2a). The characteristic peaks belonging to the (002) plane of graphitic carbon are detected at approximately 26.3° (JCPDS no. 75-1621). Additionally, the graphene-like NC in the two samples can be further validated by the presence of a prominent G band (∼1580 cm^{-1}) and D band (∼1360 cm^{-1}) in the corresponding Raman spectra (Figure 2b), which are ascribed to the E$_{2g}$ mode of sp^2-hybridized carbon.[20] Meanwhile, in the second-order region, the band at around 2700 cm^{-1} can be ascribed to the 2D band as the D-peak overtone, and another one at around 2930 cm^{-1} can be attributed to the combined overtone of the D and G bands (denoted as D + G),[21] also confirming the existence of graphene-like NC. Furthermore, the ratios of I_G/I_D for Ni/NiO@Ru-NC and Ni/NiO@NC are 1.30 and 1.35, respectively, suggesting the good crystallinity of graphite carbon synthesized by the LCVD method. Notably, the I_G/I_D of Ni/NiO@Ru-NC is relatively lower than that of Ni/NiO@NC, implying that Ru is atomically anchored in the NC matrix, inducing defects to a certain extent without destroying the main carbon lattice. More importantly, the Raman signals corresponding to the longitudinal optical (LO) mode of NiO are detected in both samples,[16] indicating the existence of NiO. Furthermore, the Raman mapping of the integrated intensity for the D peak and G peak of Ni/NiO@Ru-NC highlights the full coverage of the Ru-NC on the surface of the NF substrate (Figure 2c).[22]

To elucidate the chemical composition and valence state, Ni/NiO@Ru-NC is studied by X-ray photoelectron spectroscopy (XPS), together with the Ni/NiO@NC counterpart. In the Ni/NiO@Ru-NC, a trace amount of Ru is detected apart from the coexistence of Ni/NiO and NC (Figure 2d and Figure S7).[23] Additionally, the loading of Ru is further measured to be 2.53 wt % by inductively coupled plasma-mass spectroscopy (ICP-MS) analysis. In detail, the deconvolution of the C 1s profile of Ni/NiO@NC displays four peaks at 284.6, 285.92, 288.59, and 291.30 eV, ascribed to the C—C/C≡C, C—N, C—O, and O—C═O groups of the NC, respectively (Figure S8). Furthermore, two new peaks for Ru 3d$_{5/2}$ and Ru 3d$_{3/2}$ emerge

at 281.62 and 285.31 eV, suggesting the successful introduction of trace Ru to the Ni/NiO@Ru-NC.[24] On the other hand, the corresponding deconvoluted peaks of C—N, C—O, and O—C═O in the C 1s profile of Ni/NiO@Ru-NC display positive shifts as compared to those of Ni/NiO@NC, illustrating that the introduced Ru sites affect the electron distribution in the NC matrix.

Meanwhile, the peak in the N 1s region of Ni/NiO@NC can be deconvoluted into three peaks at 398.71, 400.87, and 403.80 eV, which are ascribed to pyridinic-N, graphitic-N, and oxidized-N, respectively (Figure S9).[25] Similarly, all peaks shift toward higher binding energies after the Ru introduction. Notably, a new peak is observed at 399.82 eV in the N 1s region of Ni/NiO@Ru-NC, ascribed to the strong coordination of N atoms to Ru sites.[26] It is consistent with the observations in the reported research works regarding the single metal sites embedded in the NC matrix.[11,27] Moreover, both high-resolution Ni 2p regions of the two samples demonstrate the coexistence of Ni and NiO (Figure S10), further confirming the generation of Janus Ni/NiO NPs coupled with the above TEM and Raman results. Specifically, for Ni/NiO@Ru-NC, two peaks at 852.60 and 870.16 eV are attributed to Ni^0; two peaks at 853.99 and 871.82 eV are assigned to Ni^{2+}; and two peaks at 855.71 and 874.03 eV are ascribed to Ni^{3+}. Moreover, there are negative shifts for the Ni 2p and O 1s peaks of Ni/NiO@Ru-NC compared with those of Ni/NiO@NC (Figure S11), also demonstrating that electron redistribution occurs due to the introduction of Ru single atoms.

To further study the local structure and coordination environment of Ru atoms, X-ray absorption near-edge structure (XANES) and extended X-ray absorption fine structure (EXAFS) studies are conducted. Figure 2e displays the XANES results at the Ru K-edge of the Ni/NiO@Ru-NC sample and the two references (i.e., Ru foil and RuO$_2$). The absorption edge position of Ni/NiO@Ru-NC is situated between that of Ru foil and RuO$_2$, manifesting that the Ru atom carries positive charges of +δ (0 < δ < 4).[28] More importantly, for Ni/NiO@Ru-NC, the Fourier-transformed (FT) k^3-weighted EXAFS spectrum exhibits one prominent peak at about 1.5 Å, which is attributed to the Ru-N coordination shell. No Ru−Ru coordination peak is detected at approximately 2.4 or 3.1 Å (Figure 2f), jointly confirming the atomic-level dispersion of Ru atoms without the formation of metallic Ru or RuO$_x$ NPs in Ni/NiO@Ru-NC.[29] Furthermore, the EXAFS data-fitting results exhibit that the coordination number of Ru-N is 4.8, demonstrating that the dominant Ru-N structure of the Ni/NiO@Ru-NC catalyst could be Ru-N$_5$ (Figure 2g and Table S1). As a result, it can be assumed that the Ru-N$_5$ pyramid structure is composed of a Ru-N$_4$ planar structure with the axial coordination of pyridinic nitrogen,[30] which is illustrated in the inset of Figure 2g and Figure S12 after optimized by DFT calculations. In addition, the wavelet transform (WT) plot of Ni/NiO@Ru-NC displays one WT maximum at around 6 Å^{-1} belonging to the Ru-N bonding as compared with Ru foil and RuO$_2$, which further indicates the isolated distribution of Ru atoms in Ni/NiO@Ru-NC (Figure 2h).[31]

Furthermore, differential charge density analysis is conducted to illustrate the electron distribution within the Ni/NiO@Ru-NC nanotube. Based on the special spatial configuration of the nanotube, the Ru-N$_5$-C model is applied to study the sidewall part and the Ni/NiO@Ru-N$_5$-C model is used to analyze the top part (Figure 2i). For the Ru-N$_5$-C configuration, an obvious
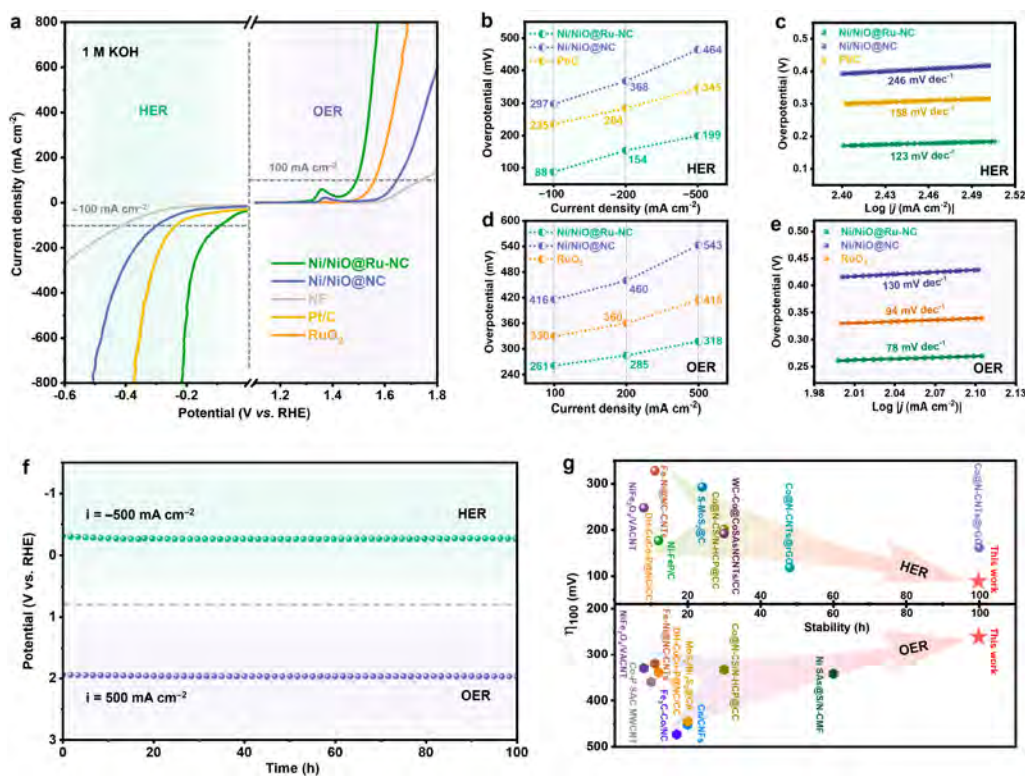
Figure 3. (a) Polarization curves, (b, d) overpotentials comparison, and (c, e) Tafel plots of tested samples for HER and OER, respectively. (f) CP curves of Ni/NiO@Ru-NC. (g) Overpotential comparison at −100/100 mA cm^{-2} with the reported carbon-supported metal-based materials.

electron redistribution occurs on the Ru atom and the adjacent N and C atoms due to the different electronegativity of atoms (Figure S13).[32] The quantitative estimation by Bader charges reveals that the metal Ru center donates electrons (1.217 e) to the adjacent N atoms, endowing the Ru center positive,[33] in agreement with the above XANES results. In this way, the electron-deficient Ru sites could serve as the active centers with regulated electron donor−acceptor properties for optimal adsorption of intermediates.[34] Besides, at the top part, for the Janus Ni/NiO NPs, a charge accumulation can be visualized at the interface between NiO and Ni, implying a built-in electric field generation at an intimately contacted heterointerface.[35] It can act as an expedited highway within the Janus Ni/NiO NPs for accelerating electron transport. Then, taking the hetero-structed Ni/NiO as a whole, when it contacts with Ru-N$_5$-C, a charge accumulation on the heterointerface occurs, demonstrating an accelerated charge transfer at the holistic top part by the construction of Janus NPs and their strong interaction with the Ru-N$_5$-C outlayer.

Alkaline HER and OER Performance. The HER activity of the Ni/NiO@Ru-NC, Ni/NiO@NC counterpart, benchmark Pt/C, and NF substrate is measured by a three-electrode system in a 1.0 M KOH solution. By tuning the Ru loading, the optimal Ni/NiO@Ru-NC sample for HER is used in subsequent tests, and the detailed results are displayed in Figures S14 and S15. As shown in the polarization curves in Figure 3a, when compared with Ni/NiO@NC (297, 368, and 464 mV) and Pt/C (235, 284, and 345 mV), Ni/NiO@Ru-NC exhibits the lowest overpotentials of 88, 154, and 199 mV in order to attain the current density of 100, 200, and 500 mA cm^{-2}, respectively (Figure 3b), displaying the best HER performance among the tested samples. Meanwhile, Ni/NiO@Ru-NC achieves the

lowest Tafel slope of 123 mV dec^{-1} in the composition of Pt/C (158 mV dec^{-1}) and Ni/NiO@NC (246 mV dec^{-1}) (Figure 3c), suggesting that the synergistic effect of Ru single atoms and Janus Ni/NiO NPs within the NC nanotubes can provide more rapid kinetics.

Moreover, the Nyquist plots in Figure S16 and corresponding fitting results in Table S2 display that Ni/NiO@Ru-NC has a lower charge transfer resistance (1.405 Ω) than that of Ni/NiO@NC (5.846 Ω). In addition, the electrochemically active surface area (ECSA) is determined by double-layer capacitance (C$_{dl}$) with cyclic voltammetry (CV) measurements. The higher C$_{dl}$ value of Ni/NiO@Ru-NC (45.1 mF cm^{-2}) than that of Ni/NiO@NC (12.9 mF cm^{-2}) demonstrates there are much more catalytically active sites generated in Ni/NiO@Ru-NC for H$_2$ evolution (Figure S17).[36] Therefore, these experimental results substantiate that the imported Ru single sites accompanied by the tip Ni/NiO NPs contribute to promoting the charge transfer and increasing the density of active sites for the whole array system, which is coincident with the calculated results from differential charge density.

Afterward, a chronopotentiometry (CP) test is conducted to evaluate the durability of Ni/NiO@Ru-NC for the HER activity at −500 mA cm^{-2}. The potential is rather stable with negligible fluctuation in the strong reducing environment for 100 h (Figure 3f), suggesting that the Ni/NiO@Ru-NC has good durability toward HER in an alkaline solution. On the other hand, the morphology of the long-term-tested sample observed from the SEM image is well-maintained in the nanotube structure with interconnected networks as open channels for the gas release so that it features good structural integrity (Figure S18). The corresponding XRD result displays a pattern identical to the original Ni/NiO@Ru-NC sample (Figure S19). Furthermore,
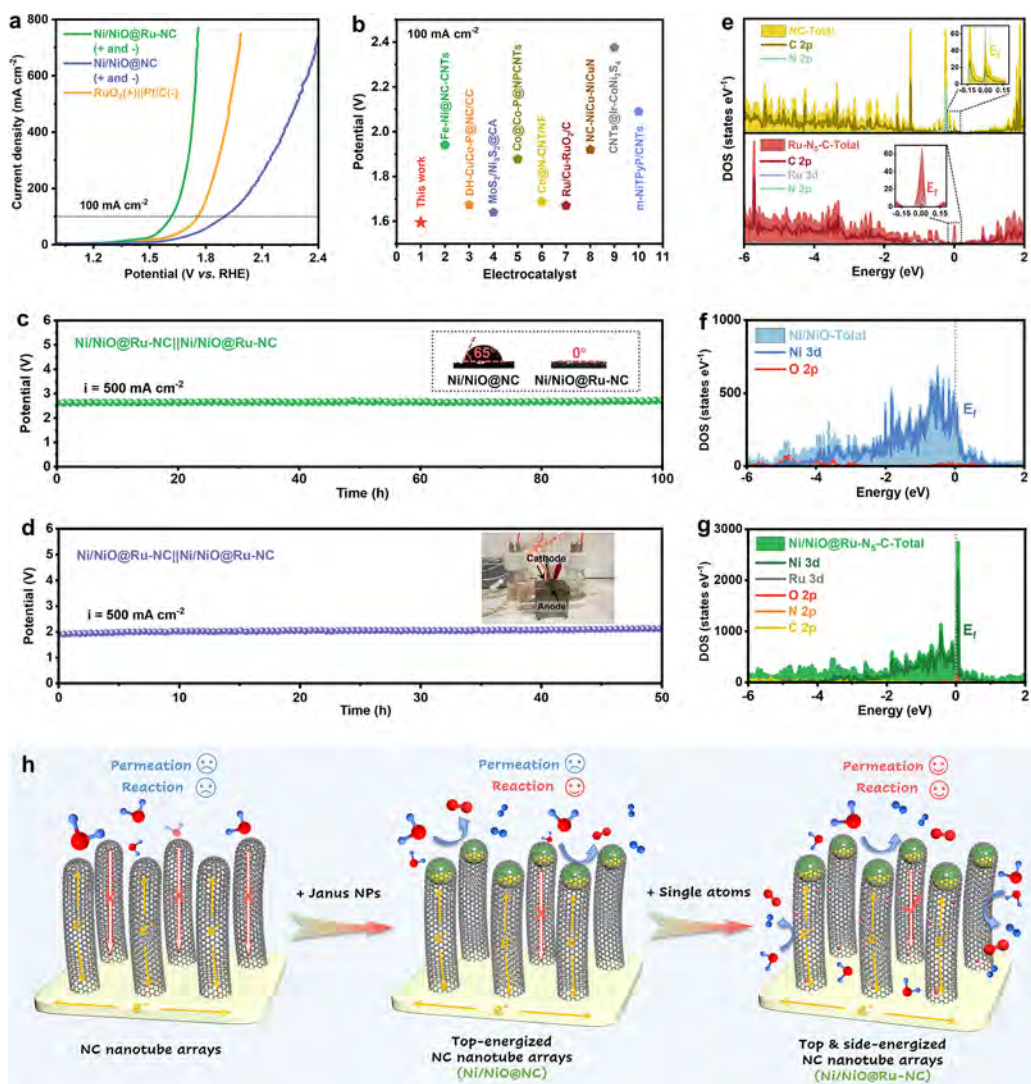
Figure 4. (a) Polarization curves and (b) potential comparison with the reported carbon-based materials for overall water splitting. CP curves of the bifunctional Ni/NiO@Ru-NC electrode (c) in the traditional two-electrode configuration and (d) in the AEMWE system at 500 mA cm^{-2} (inset of c, contact angle; inset of d, a photograph of the AEMWE system). TDOS and PDOS of (e) NC and Ru-N$_5$-C, (f) Ni/NiO, and (g) Ni/NiO@Ru-N$_5$-C. (h) Schematic illustration of the functional mechanism for NC, Ni/NiO@NC, and Ni/NiO@Ru-NC.

the XPS results of Ni/NiO@Ru-NC subjected to the HER stability test reveal the coexistence of Ru, Ni (Ni^{3+}/Ni^{2+}/Ni^0), O, N, and C elements, implying the elemental stability under the shielding with a robust carbon sheath (Figure S20). Particularly, the alkaline HER activity and stability of Ni/NiO@Ru-NC surpass most reported carbon-based materials, ranking the top tier among the state-of-the-art carbon-supported metal-based electrocatalysts for alkaline HER reported to date (Figure 3g and Table S3).

In the following, to investigate their OER performance, the Ni/NiO@Ru-NC, Ni/NiO@NC, NF substrate, and RuO$_2$ as the benchmark samples are tested via the three-electrode system in the 1.0 M KOH solution. Similarly, the optimal Ni/NiO@Ru-NC sample for the OER is used in subsequent tests after tuning the Ru loading, and the detailed result is shown in Figure S21. As depicted in Figure 3a, the corresponding polarization curves demonstrate that Ni/NiO@Ru-NC features the best electrocatalytic OER activity among the tested electrocatalysts. In the comparison of Ni/NiO@NC (416, 460, and 543 mV) and RuO$_2$ (330, 360, and 415 mV), Ni/NiO@Ru-NC requires low

overpotentials of 261, 285, and 318 mV to achieve the current density of 100, 200, and 500 mA cm^{-2}, respectively (Figure 3d). Meanwhile, Ni/NiO@Ru-NC displays a smaller Tafel slope (78 mV dec^{-1}) than RuO$_2$ (94 mV dec^{-1}) and Ni/NiO@NC (130 mV dec^{-1}) (Figure 3e), demonstrating that the introduction of single-atom Ru and Janus Ni/NiO NPs also synergistically accelerates the OER kinetics.[2] Furthermore, as revealed by the Nyquist plots (Figure S22) and corresponding fitting results (Table S4), the Ni/NiO@Ru-NC displays a lower charge transfer resistance (1.019 Ω) than the Ni/NiO@NC (8.806 Ω). The Ni/NiO@Ru-NC delivers a C$_{dl}$ value of 24.5 mF cm^{-2}, which is larger than that of Ni/NiO@NC (11.4 mF cm^{-2}) (Figure S23). More importantly, Ni/NiO@Ru-NC exhibits good stability by sustaining 500 mA cm^{-2} for 100 h with a negligible change of potential in 1.0 M KOH solution (Figure 3f). The SEM image, XRD pattern, and XPS results for the Ni/NiO@Ru-NC subjected to the OER activity also reveal the well-maintained morphology and composition, further demonstrating the good durability of Ni/NiO@Ru-NC under the protection of a robust carbon matrix (Figures S24−26). As a

result, such good activity and stability of Ni/NiO@Ru-NC for alkaline OER are also among the best-reported values for carbon-supported metal-based OER electrocatalysts by far (Figure 3g and Table S5).

Overall Water Splitting Application and Mechanism Exploration. Encouraged by the good HER and OER performance, a two-electrode configuration electrolyzer for the overall water splitting application is integrated by the Ni/NiO@Ru-NC catalyst as both the anode and cathode in 1.0 M KOH solution. This electrolyzer is denoted as Ni/NiO@Ru-NC‖Ni/NiO@Ru-NC. In comparison, the Ni/NiO@NC‖Ni/NiO@NC and RuO$_2$‖Pt/C two-electrode configurations are also built and measured. As revealed in Figure 4a, the Ni/NiO@Ru-NC‖Ni/NiO@Ru-NC can afford 100 mA cm^{-2} only at the operating potential of 1.595 V, which is much superior to those of RuO$_2$‖Pt/C (1.758 V) and Ni/NiO@NC‖Ni/NiO@NC (1.899 V). Also, Ni/NiO@Ru-NC‖Ni/NiO@Ru-NC can reach 200 and 500 mA cm^{-2} at 1.667 and 1.734 V, respectively (Figure S27). Notably, this performance is also superior to most reported carbon-based bifunctional electrocatalysts (Figure 4b and Table S6). Moreover, the durability of this Ni/NiO@Ru-NC‖Ni/NiO@Ru-NC electrolyzer is evaluated at 500 mA cm^{-2}. The corresponding CP curve in Figure 4c demonstrates that Ni/NiO@Ru-NC‖Ni/NiO@Ru-NC exhibits a steady cell voltage for 100 h, confirming the good robustness of Ni/NiO@Ru-NC for overall water splitting. Furthermore, encouraged by the good activity and stability of Ni/NiO@Ru-NC in the two-electrode configuration, it is integrated into an AEMWE system to reduce the ohmic loss during the electrocatalytic water-splitting process (inset, Figure 4d). Similarly, in the compact AEMWE electrolyzer, the self-supported Ni/NiO@Ru-NC electrode, without using an ionomer, can act as an efficient and robust bifunctional catalyst with porous transport layers to operate stably for 50 h under 500 mA cm^{-2} at a voltage of 1.95 ± 0.05 V in 1.0 M KOH at room temperature, further indicating its good bifunctional performance and great potentials for practical applications (Figure 4d).

To disclose the underlying mechanism for the high electrocatalytic performance of the Ni/NiO@Ru-NC electrocatalyst, the total density of states (TDOS) and the partial density of states (PDOS) of NC, Ru-N$_5$-C, Ni/NiO, and Ni/NiO@Ru-N$_5$-C are calculated to study the intrinsic electronic structures. The NC model is applied as the optimized two-layer carbon with pyridinic nitrogen to compare with the Ru-N$_5$-C configuration (Figure S28). As displayed in Figure 4e, the confinement of Ru single atoms into NC generates higher electronic states near the Fermi level than that of NC because of the strongly coupled orbitals between the Ru 3d orbitals and the neighboring N 2p and C 2p orbitals, leading to a more conductive electronic structure.[37] Combining the results of differential charge density, the incorporation of Ru single atoms can regulate the electron distribution by strong d−p orbital couplings to activate the Ru-N$_5$-C domains with faster charge transfer, thus energizing the sidewalls of NC nanotubes for electrocatalytic reactions. On the other hand, in Figure 4f, the Janus Ni/NiO has a band gap of zero as the substantial electronic states cross the Fermi energy (E_f). After the Ni/NiO is hybridized with Ru-N$_5$-C (Figure 4g), the Ni/NiO@Ru-N$_5$-C presents significantly higher PDOS states than that of Ni/NiO and Ru-N$_5$-C at the vicinity of the Fermi level, which demonstrates that the intimate heterointerface construction can regulate the orbital couplings with facilitated electron transfer, accelerating the reaction kinetics at the top part.[38] In this regard, stringing single Ru atoms and

Janus Ni/NiO NPs can synergistically energize the NC nanotubes from sidewalls to tops with strong orbital couplings to facilitate charge transfer, prominently improving the reaction kinetics of the NC nanotube for electrocatalytic overall water splitting.

To better understand the advantages of multiscale confinement engineering in nanotube arrays, three cascaded models are proposed to illustrate the electrochemical process progressively, i.e., NC nanotube arrays, Ni/NiO@NC nanotube arrays, and Ni/NiO@Ru-NC nanotube arrays, respectively (Figure 4h). In principle, the surface of carbon is hydrophobic, preventing the permeation of OH$^-$/H$^+$, H$_2$O, and electrolytes. With an inferior mass diffusion, the electrolyte can only contact the apex of NC nanotube arrays. However, the NC lacks valid active sites to proceed with electrocatalytic HER and OER efficiently. In this regard, after introducing Janus Ni/NiO NPs within the apical domains of the NC nanotube, the top part of the Ni/NiO@NC nanotubes with the construction of heterointerfaces could provide more active sites and favorable charge transport at the reactant-accessible apex of the nanotube arrays, thus accelerating the HER/OER processes as compared with those of pristine NC nanotube arrays. However, the electrolyte is still hard to permeate into the base of NC nanotube arrays, which limits the full play of whole NC nanotube arrays. In this case, when the Ru single atoms are imported into the NC matrix along with the apical Ni/NiO NPs, the NC nanotube arrays can be fully energized from top to sidewalls. Specifically, the formed Ru-NC can be more hydrophilic than the primitive NC for superior mass diffusion and can also significantly increase the density of active sites at the sidewalls. The promoted hydrophilic property of Ni/NiO@Ru-NC is proved by contact angle measurements. The water contact angle for Ni/NiO@NC is 65°. Meanwhile, when a droplet gets in touch with the surface of Ni/NiO@Ru-NC, it spreads quickly (i.e., the contact angle is close to 0°), signifying a substantial enhancement in hydrophilicity after the introduction of single Ru atoms (inset, Figure 4c). Therefore, the electrolyte can easily permeate into the base of Ni/NiO@Ru-NC nanotube arrays with good mass diffusion. The HER/OER processes can be further proceeded through the whole array system, not limited to the apical domains. Moreover, the flexible nanotube arrays forming different porosities can provide channels to rapidly release gaseous products, circumventing the structural destruction due to bubble accumulation at the base.

Taken together, our one-step LCVD method simultaneously confining Ru single atoms and Janus Ni/NiO NPs within NC nanotube arrays can be illustrated as one stone with three birds: (i) providing abundant active sites from top to sidewalls; (ii) regulating the electronic distribution to accelerate the electron transfer; (iii) increasing the hydrophilicity to facilitate the permeation of OH$^-$/H$^+$, H$_2$O, and electrolytes into the whole array system. Besides, the flexible nanotube arrays featuring porous channels can accelerate the generated gas bubble to detach from the active sites to reinforce their mechanical stability. Consequently, the Ni/NiO@Ru-NC nanotube arrays feature good activity and stability for overall water spitting.

To further illustrate the feasibility of Ni/NiO@Ru-NC for potential practical application, the solar-driven water-splitting electrolyzer is constructed by the Ni/NiO@Ru-NC‖Ni/NiO@Ru-NC setup integrated with a silicon solar cell (Figure S29a). It is observed that enormous bubbles with a small size continuously generate and rapidly release from the two electrodes (Figure S29b and Movie S1), which demonstrates that the Ni/NiO@Ru-NC‖Ni/NiO@Ru-NC couple having a

fast mass transfer can be efficiently driven by a commercial solar panel under sunlight irradiation. Therefore, it is indicated that Ni/NiO@Ru-NC can act as an efficient bifunctional electrocatalyst for potential industrial applications.

CONCLUSION

In summary, the Ni/NiO@Ru-NC nanotube arrays are synthesized by multiscale confinement engineering using a simple one-step LCVD strategy, which simultaneously introduces single Ru atoms into the sidewalls and Janus Ni/NiO NPs at the apical domains to fully energize the NC nanotube arrays by regulating the electronic distribution. As a result, the Ni/NiO@Ru-NC exhibits good bifunctional HER and OER performance with long-term durability at high current densities, which can be ascribed to the accelerated charge transfer, improved mass diffusion, enriched active sites, and porous open channels derived from the flexible nanotube arrays. Specifically, the Ni/NiO@Ru-NC affords overpotentials of 88 and 199 mV at −100 and −500 mA cm^{-2} for alkaline HER, respectively, and overpotentials of 261 and 318 mV at 100 and 500 mA cm^{-2} for alkaline OER, respectively, both of which rank the top tier among reported carbon-supported metal-based materials. Moreover, Ni/NiO@Ru-NC drives the overall water-splitting to achieve 100 and 500 mA cm^{-2} at cell voltages of 1.595 and 1.734 V, respectively. An overall water-splitting electrolyzer can be efficiently driven by a solar cell, and an AEMWE system can be stably operated under 500 mA cm^{-2} for 50 h, demonstrating its great potential for practical applications.

EXPERIMENTAL SECTION

Chemicals and Materials. Acetonitrile (CH$_3$CN) was purchased from RCI Labscan Ltd. Ruthenium trichloride hydrate (RuCl$_3$·xH$_2$O) was purchased from Sigma-Aldrich Co., Ltd. Potassium hydroxide (KOH) was purchased from Meryer Chemical Technology CO., Ltd. Nickel foam (NF) and anion exchange membrane (AEM, Dioxide Materials Sustainion X37-50RT) were purchased from Fuel Cell Store Co. Deionized water (DI water) was obtained from local sources.

The Pretreatment of NF. The NF (thickness: 2 mm) was cut into rectangular pieces with a size of 2 × 3 cm^2. The NF pieces were immersed into 0.5 M H$_2$SO$_4$ solution for 15 min. Then, they were cleaned by sequential sonication treatment in acetone, ethanol, and DI water for 15 min each. Finally, the NF pieces were dried at 60 °C in the oven.

Synthesis of Ni/NiO@Ru-NC. One pretreated NF piece was put in the quartz tube center. A gas washing bottle containing 100 mL of CH$_3$CN solution and 10 mg of RuCl$_3$·xH$_2$O is connected to the air inlet of the tube furnace. Argon (Ar) flow was employed at 100 sccm to pass through the solution to create a CH$_3$CN/RuCl$_3$/Ar atmosphere. Next, the NF was calcinated at 700 °C for 2 h (ramping rate: 5 °C min^{-1}) to form the final product Ni/NiO@Ru-NC.

Synthesis of Ni/NiO@NC. Except for being without the addition of RuCl$_3$·xH$_2$O, the synthesis procedure of Ni/NiO@NC was the same as that of Ni/NiO@Ru-NC.

Characterizations. SEM was performed by using the FEI Quanta 450 equipment. TEM, HRTEM, HAADF-STEM, element mapping analysis, and line scans were carried out by using a JEM-2100F instrument. The AC-STEM was conducted by applying a Thermo Fisher Scientific Spectra 300 S/TEM at an accelerating voltage of 300 kV. XPS was carried out on Thermo Fisher ESCALAB 250Xi equipment. Raman measurement was carried out on a WITec alpha300 R Raman System with a laser wavelength of 532 nm. Raman mapping was performed across a surface area of 1.0 × 1.0 μm^2. XRD patterns were collected on a Rigaku SmartLab high-resolution X-ray diffractometer. The contact angle was tested by a Data Physics Contact Angle Tester. ICP-MS was conducted on a PE optima 6000 spectrometer. The characterization of the X-ray absorption fine

structure (XAFS) was conducted at the Shanghai Synchrotron Radiation Facility (SSRF). The Ru K-edge XAFS analyses were performed with Si(311) crystal monochromators at the BL14W Beamline. The samples were placed into aluminum sample holders and sealed with a Kapton tape film before the analysis at the beamline. The XAFS spectra were collected at room temperature using a four-channel silicon drift detector (SDD) Bruker 5040. Ru K-edge EXAFS spectra were recorded in the fluorescence mode. Meanwhile, the XAFS spectra of the reference samples were recorded in transmission mode. The Athena program is used for the process and analysis of the raw spectra obtained.

Preparation of Pt/C and RuO$_2$ Inks. Five mg of Pt/C (commercial 20% Pt/C) or RuO$_2$ was dispersed into 500 μL of mixture solution (50 μL of 5 wt % Nafion and 450 μL of ethanol) under sonication treatment for 2 h to obtain a homogeneous ink. Finally, we drop-casted 50 μL of ink onto the NF surface (0.5 × 1 cm^2; mass loading: 1 mg cm^{-2}).

Electrochemical Tests. A standard three-electrode setup on an electrochemical workstation (CHI 760E) is applied to conduct all electrochemical measurements. Besides, the AEMWE system was controlled by an electrochemical workstation (CHI 660E) with a high-current amplifier (CHI 680C). M KOH (1.0 M) is used as an electrolyte (pH = 13.68). The catalyst/NF samples were directly employed as a working electrode with 0.5 cm^2 (*i.e.*. 0.5 cm × 1 cm) for the reactions. The counter electrode is a graphite rod. The reference electrode is a Ag/AgCl electrode.

The electrolyte was bubbled with an Ar flow for 30 min before the electrochemical measurement. Numerous CV cycles were applied to activate the electrocatalysts until they remained stable. The linear sweep voltammetry (LSV) curves were collected with a scan rate of 5 mV s^{-1}. Unless otherwise mentioned, all polarization curves were exhibited with *iR* correction based on the formula $E_{iR} = E_0 - i \times R_s$. R_s represents solution resistance obtained from electrochemical impedance spectroscopy (EIS). EIS measurement was carried out with a frequency range from 100,000 to 0.01 Hz and an amplitude of 5 mV at −0.23 V vs RHE for HER and at 1.52 V vs RHE for OER. CV curves were collected at different scan rates in the potential range from 0.10 to 0.20 vs RHE to evaluate the C_{dl} values for HER and from 1.00 to 1.10 vs RHE for OER. The CP test is applied at −500/500 mA cm^{-2} for HER/OER without *iR* compensation to evaluate the long-term stability. A two-electrode configuration is employed for the overall water-splitting test, and the corresponding long-term stability test was assessed by CP test at 500 mA cm^{-2} without *iR* compensation in 1.0 M KOH solution. In addition, 1 mL of electrolyte was periodically added into the long-term-tested system every 24 h. The Nernst equation is used to normalize all potentials to the RHE reference scale: E (vs RHE) = E (vs Ag/AgCl) + 0.197 V + 0.0591 V × pH.

Theoretical Computation Details. The first principal calculation based on DFT is realized by Vienna Ab-initio Simulation Package (VASP) code[39,40] with the full-potential projected augmented wave (PAW) formalism.[41] The generalized gradient approximation (GGA) under the Perdew−Burke−Ernzerhof (PBE) formalism was applied to describe exchange correlation.[42] Grimme's DFT-D2 functional is used to evaluate the dispersive van der Waals interactions between composites. A vacuum layer of 20 Å is applied to avoid perturbations from neighboring layers. The cutoff energy for the plane-wave expansion is set to 450 eV. A convergence criterion of 10^{-5} eV is set for self-consistence, and the structure is relaxed until the maximum stress on each atom is lower than 0.01 eV/Å. The Γ-centered k-point mesh of 4 × 4 × 1 is used for the DOS calculation.

ASSOCIATED CONTENT

Ⓢ Supporting Information

The Supporting Information is available free of charge at https://pubs.acs.org/doi/10.1021/acsnano.3c11705.

Schematic of the LCVD system; line scanning profiles; SEM, TEM, and HRTEM images of Ni/NiO@NC; SEM images and corresponding elemental mapping for pre-

treated NF; SEM images of the obtained materials by time-dependent control experiments; schematic illustration of the growth mechanism; XPS spectra; the Ru-N$_5$-C and NC configuration; differential charge density of Ru-N$_5$-C; polarization curves of Ni/NiO@Ru-NC with different amounts of RuCl$_3$·xH$_2$O for HER and OER; aberration-corrected STEM images of Ni/NiO@Ru-NC-100Ru; Nyquist plots; CV curves and corresponding C$_{dl}$ value; cross-sectional SEM images, XRD, and XPS spectra of Ni/NiO@Ru-NC after HER and OER stability test; digital photograph of the electrolyzer driven by a silicon solar cell; tables for EXAFS fitting parameters, performance comparison, and fitting results of EIS spectra (PDF)

Movie S1 showing the Ni/NiO@Ru-NC‖Ni/NiO@Ru-NC couple for overall water splitting driven by a solar cell under sunlight irradiation in 1 M KOH (MP4)

AUTHOR INFORMATION

Corresponding Authors

Shaohai Li − *Shenzhen Geim Graphene Center, Tsinghua-Berkeley Shenzhen Institute & Institute of Materials Research, Tsinghua Shenzhen International Graduate School, Tsinghua University, Shenzhen 518055, China*; Email: lishaohai@sz.tsinghua.edu.cn

Johnny C. Ho − *Department of Materials Science and Engineering, City University of Hong Kong, Hong Kong SAR 999077, China; Institute for Materials Chemistry and Engineering, Kyushu University, Fukuoka 816-8580, Japan; State Key Laboratory of Terahertz and Millimeter Waves, City University of Hong Kong, Hong Kong SAR 999077, China*; orcid.org/0000-0003-3000-8794; Email: johnnyho@cityu.edu.hk

Authors

Quan Quan − *Department of Materials Science and Engineering, City University of Hong Kong, Hong Kong SAR 999077, China*

Yuxuan Zhang − *Department of Materials Science and Engineering, City University of Hong Kong, Hong Kong SAR 999077, China*

SenPo Yip − *Institute for Materials Chemistry and Engineering, Kyushu University, Fukuoka 816-8580, Japan*

Wei Wang − *Department of Materials Science and Engineering, City University of Hong Kong, Hong Kong SAR 999077, China; State Key Laboratory of Terahertz and Millimeter Waves, City University of Hong Kong, Hong Kong SAR 999077, China*

Pengshan Xie − *Department of Materials Science and Engineering, City University of Hong Kong, Hong Kong SAR 999077, China*

Dong Chen − *Department of Materials Science and Engineering, City University of Hong Kong, Hong Kong SAR 999077, China*

Weijun Wang − *Department of Materials Science and Engineering, City University of Hong Kong, Hong Kong SAR 999077, China*

Di Yin − *Department of Materials Science and Engineering, City University of Hong Kong, Hong Kong SAR 999077, China*

Yezhan Li − *Department of Materials Science and Engineering, City University of Hong Kong, Hong Kong SAR 999077, China*

Bilu Liu − *Shenzhen Geim Graphene Center, Tsinghua-Berkeley Shenzhen Institute & Institute of Materials Research, Tsinghua*

Shenzhen International Graduate School, Tsinghua University, Shenzhen 518055, China; orcid.org/0000-0002-7274-5752

Complete contact information is available at:
https://pubs.acs.org/10.1021/acsnano.3c11705

Notes

The authors declare no competing financial interest.

REFERENCES

(1) Cheng, F.; Peng, X.; Hu, L.; Yang, B.; Li, Z.; Dong, C. L.; Chen, J. L.; Hsu, L. C.; Lei, L.; Zheng, Q.; Qiu, M.; Dai, L.; Hou, Y. Accelerated Water Activation and Stabilized Metal-organic Framework via Constructing Triangular Active-regions for Ampere-level Current Density Hydrogen Production. *Nat. Commun.* **2022**, *13*, 6486.

(2) Li, P.; Wang, M.; Duan, X.; Zheng, L.; Cheng, X.; Zhang, Y.; Kuang, Y.; Li, Y.; Ma, Q.; Feng, Z.; Liu, W.; Sun, X. Boosting Oxygen Evolution of Single-atomic Ruthenium through Electronic Coupling with Cobalt-iron Layered Double Hydroxides. *Nat. Commun.* **2019**, *10*, 1711.

(3) Wang, Y.; Wang, S.; Ma, Z. L.; Yan, L. T.; Zhao, X. B.; Xue, Y. Y.; Huo, J. M.; Yuan, X.; Li, S. N.; Zhai, Q. G. Competitive Coordination-Oriented Monodispersed Ruthenium Sites in Conductive MOF/LDH Hetero-Nanotree Catalysts for Efficient Overall Water Splitting in Alkaline Media. *Adv. Mater.* **2022**, *34*, No. e2107488.

(4) Xu, H.; Shan, C.; Wu, X.; Sun, M.; Huang, B.; Tang, Y.; Yan, C.-H. Fabrication of Layered Double Hydroxide Microcapsules Mediated by Cerium Doping in Metal−organic Frameworks for Boosting Water Splitting. *Energy Environ. Sci.* **2020**, *13*, 2949−2956.

(5) Li, S.-H.; Qi, M.-Y.; Tang, Z.-R.; Xu, Y.-J. Nanostructured Metal Phosphides: from Controllable Synthesis to Sustainable Catalysis. *Chem. Soc. Rev.* **2021**, *50*, 7539−7586.

(6) Li, S.-H.; Zhang, N.; Xie, X.; Luque, R.; Xu, Y.-J. Stress-transfer-induced In Situ Formation of Ultrathin Nickel Phosphide Nanosheets for Efficient Hydrogen Evolution. *Angew. Chem., Int. Ed.* **2018**, *57*, 13082−13085.

(7) Lei, C.; Wang, Y.; Hou, Y.; Liu, P.; Yang, J.; Zhang, T.; Zhuang, X.; Chen, M.; Yang, B.; Lei, L.; Yuan, C.; Qiu, M.; Feng, X. Efficient Alkaline Hydrogen Evolution on Atomically Dispersed Ni−N$_x$ Species Anchored Porous Carbon with Embedded Ni Nanoparticles by Accelerating Water Dissociation Kinetics. *Energy Environ. Sci.* **2019**, *12*, 149−156.

(8) Xie, X.; He, C.; Li, B.; He, Y.; Cullen, D. A.; Wegener, E. C.; Kropf, A. J.; Martinez, U.; Cheng, Y.; Engelhard, M. H.; Bowden, M. E.; Song, M.; Lemmon, T.; Li, X. S.; Nie, Z.; Liu, J.; Myers, D. J.; Zelenay, P.; Wang, G.; Wu, G.; Ramani, V.; Shao, Y. Performance Enhancement and Degradation Mechanism Identification of A Single-atom Co−N−C Catalyst for Proton Exchange Membrane Fuel Cells. *Nat. Catal.* **2020**, *3*, 1044−1054.

(9) Zhao, D.; Sun, K.; Cheong, W. C.; Zheng, L.; Zhang, C.; Liu, S.; Cao, X.; Wu, K.; Pan, Y.; Zhuang, Z.; Hu, B.; Wang, D.; Peng, Q.; Chen, C.; Li, Y. Synergistically Interactive Pyridinic-N-MoP Sites: Identified Active Centers for Enhanced Hydrogen Evolution in Alkaline Solution. *Angew. Chem., Int. Ed.* **2020**, *59*, 8982−8990.

(10) Tong, Y.; Liu, J.; Wang, L.; Su, B. J.; Wu, K. H.; Juang, J. Y.; Hou, F.; Yin, L.; Dou, S. X.; Liu, J.; Liang, J. Carbon-Shielded Single-Atom Alloy Material Family for Multi-Functional Electrocatalysis. *Adv. Funct. Mater.* **2022**, *32*, 2205654.

(11) Li, Y.; Ji, Y.; Zhao, Y.; Chen, J.; Zheng, S.; Sang, X.; Yang, B.; Li, Z.; Lei, L.; Wen, Z.; Feng, X.; Hou, Y. Local Spin-state Tuning of Iron Single-atom Electrocatalyst by S-coordinated Doping for Kinetics-boosted Ammonia Synthesis. *Adv. Mater.* **2022**, *34*, No. e2202240.

(12) Hou, Y.; Qiu, M.; Kim, M. G.; Liu, P.; Nam, G.; Zhang, T.; Zhuang, X.; Yang, B.; Cho, J.; Chen, M.; Yuan, C.; Lei, L.; Feng, X. Atomically Dispersed Nickel-nitrogen-sulfur Species Anchored on Porous Carbon Nanosheets for Efficient Water Oxidation. *Nat. Commun.* **2019**, *10*, 1392.

(13) Cui, X.; Gao, L.; Lei, S.; Liang, S.; Zhang, J.; Sewell, C. D.; Xue, W.; Liu, Q.; Lin, Z.; Yang, Y. Simultaneously Crafting Single-atomic Fe Sites and Graphitic Layer-wrapped Fe₃C Nanoparticles Encapsulated within Mesoporous Carbon Tubes for Oxygen Reduction. *Adv. Funct. Mater.* **2021**, *31*, 2009197.

(14) Quan, Q.; Bu, X.; Chen, D.; Wang, F.; Kang, X.; Wang, W.; Meng, Y.; Yip, S.; Liu, C.; Ho, J. C. Sequential Self-reconstruction of Localized Mo Species in Hierarchical Carbon/Co–Mo Oxide Heterostructures for Boosting Alkaline Hydrogen Evolution Kinetics and Durability. *J. Mater. Chem. A* **2022**, *10*, 3953–3962.

(15) Lin, J.; Zeng, C.; Lin, X.; Xu, C.; Xu, X.; Luo, Y. Metal-organic Framework-derived Hierarchical MnO/Co with Oxygen Vacancies toward Elevated-Temperature Li-Ion Battery. *ACS Nano* **2021**, *15*, 4594–4607.

(16) Quan, Q.; Zhang, T.; Lei, C.; Yang, B.; Li, Z.; Chen, J.; Yuan, C.; Lei, L.; Hou, Y. Confined Carburization-Engineered Synthesis of Ultrathin Nickel Oxide/Nickel Heterostructured Nanosheets for Enhanced Oxygen Evolution Reaction. *Nanoscale* **2019**, *11*, 22261–22269.

(17) Tao, H.; Choi, C.; Ding, L.-X.; Jiang, Z.; Han, Z.; Jia, M.; Fan, Q.; Gao, Y.; Wang, H.; Robertson, A. W.; Hong, S.; Jung, Y.; Liu, S.; Sun, Z. Nitrogen Fixation by Ru Single-Atom Electrocatalytic Reduction. *Chem.* **2019**, *5*, 204–214.

(18) Aijaz, A.; Masa, J.; Rösler, C.; Xia, W.; Weide, P.; Botz, A. J. R.; Fischer, R. A.; Schuhmann, W.; Muhler, M. Co@Co₃O₄ Encapsulated in Carbon Nanotube-Grafted Nitrogen-Doped Carbon Polyhedra as an Advanced Bifunctional Oxygen Electrode. *Angew. Chem., Int. Ed.* **2016**, *55*, 4087–4091.

(19) Gong, W.; Lin, Y.; Chen, C.; Al-Mamun, M.; Lu, H.-S.; Wang, G.; Zhang, H.; Zhao, H. Nitrogen-doped Carbon Nanotube Confined Co–Nₓ Sites for Selective Hydrogenation of Biomass-derived Compounds. *Adv. Mater.* **2019**, *31*, 1808341.

(20) Cheng, Y.; Gong, J.; Cao, B.; Xu, X.; Jing, P.; Liu, B.; Gao, R.; Zhang, J. An Ingenious Strategy to Integrate Multiple Electrocatalytically Active Components within a Well-Aligned Nitrogen-Doped Carbon Nanotube Array Electrode for Electrocatalysis. *ACS Catal.* **2021**, *11*, 3958–3974.

(21) Ferrari, A. C.; Basko, D. M. Raman Spectroscopy as A Versatile Tool for Studying the Properties of Graphene. *Nat. Nanotechnol.* **2013**, *8*, 235–246.

(22) Chen, K.; Zhou, X.; Cheng, X.; Qiao, R.; Cheng, Y.; Liu, C.; Xie, Y.; Yu, W.; Yao, F.; Sun, Z.; Wang, F.; Liu, K.; Liu, Z. Graphene Photonic Crystal Fibre with Strong and Tunable Light–matter Interaction. *Nat. Photonics* **2019**, *13*, 754–759.

(23) Cui, X.; Gao, L.; Lei, S.; Liang, S.; Zhang, J.; Sewell, C. D.; Xue, W.; Liu, Q.; Lin, Z.; Yang, Y. Simultaneously Crafting Single-Atomic Fe Sites and Graphitic Layer-Wrapped Fe₃C Nanoparticles Encapsulated within Mesoporous Carbon Tubes for Oxygen Reduction. *Adv. Funct. Mater.* **2021**, *31*, 2009197.

(24) Xiao, M.; Gao, L.; Wang, Y.; Wang, X.; Zhu, J.; Jin, Z.; Liu, C.; Chen, H.; Li, G.; Ge, J.; He, Q.; Wu, Z.; Chen, Z.; Xing, W. Engineering Energy Level of Metal Center: Ru Single-Atom Site for Efficient and Durable Oxygen Reduction Catalysis. *J. Am. Chem. Soc.* **2019**, *141*, 19800–19806.

(25) Ao, X.; Zhang, W.; Li, Z.; Li, J.-G.; Soule, L.; Huang, X.; Chiang, W.-H.; Chen, H. M.; Wang, C.; Liu, M.; Zeng, X. C. Markedly Enhanced Oxygen Reduction Activity of Single-Atom Fe Catalysts via Integration with Fe Nanoclusters. *ACS Nano* **2019**, *13*, 11853–11862.

(26) Chen, S.; Zhou, Y.; Li, J.; Hu, Z.; Dong, F.; Hu, Y.; Wang, H.; Wang, L.; Ostrikov, K. K.; Wu, Z. Single-atom Ru-implanted Metal–organic Framework/MnO₂ for the Highly Selective Oxidation of NOₓ by Plasma Activation. *ACS Catal.* **2020**, *10*, 10185–10196.

(27) Wang, X.; Wang, Y.; Sang, X.; Zheng, W.; Zhang, S.; Shuai, L.; Yang, B.; Li, Z.; Chen, J.; Lei, L.; Adli, N. M.; Leung, M. K. H.; Qiu, M.; Wu, G.; Hou, Y. Dynamic Activation of Adsorbed Intermediates via Axial Traction for the Promoted Electrochemical CO₂ Reduction. *Angew. Chem., Int. Ed.* **2021**, *60*, 4192–4198.

(28) Qin, Y.; Guo, C.; Ou, Z.; Xu, C.; Lan, Q.; Jin, R.; Liu, Y.; Niu, Y.; Xu, Q.; Si, Y.; Li, H. Regulating Single-atom Mn Sites by Precisely Axial Pyridinic-nitrogen Coordination to Stabilize the Oxygen Reduction. *J. Energy Chem.* **2023**, *80*, 542–552.

(29) Qi, H.; Yang, J.; Liu, F.; Zhang, L.; Yang, J.; Liu, X.; Li, L.; Su, Y.; Liu, Y.; Hao, R.; Wang, A.; Zhang, T. Highly Selective and Robust Single-atom Catalyst Ru₁/NC for Reductive Amination of Aldehydes/Ketones. *Nat. Commun.* **2021**, *12*, 3295.

(30) Zhang, H.; Li, J.; Xi, S.; Du, Y.; Hai, X.; Wang, J.; Xu, H.; Wu, G.; Zhang, J.; Lu, J.; Wang, J. A Graphene-Supported Single-Atom FeN₅ Catalytic Site for Efficient Electrochemical CO₂ Reduction. *Angew. Chem., Int. Ed.* **2019**, *58*, 14871–14876.

(31) Xue, D.; Yuan, P.; Jiang, S.; Wei, Y.; Zhou, Y.; Dong, C.-L.; Yan, W.; Mu, S.; Zhang, J.-N. Altering the Spin State of Fe-N-C Through Ligand Field Modulation of Single-atom Sites Boosts the Oxygen Reduction Reaction. *Nano Energy* **2023**, *105*, No. 108020.

(32) Kuang, P.; Wang, Y.; Zhu, B.; Xia, F.; Tung, C.-W.; Wu, J.; Chen, H. M.; Yu, J. Pt Single Atoms Supported on N-doped Mesoporous Hollow Carbon Spheres with Enhanced Electrocatalytic H₂-Evolution Activity. *Adv. Mater.* **2021**, *33*, 2008599.

(33) Kumar, A.; Bui, V. Q.; Lee, J.; Wang, L.; Jadhav, A. R.; Liu, X.; Shao, X.; Liu, Y.; Yu, J.; Hwang, Y.; Bui, H. T. D.; Ajmal, S.; Kim, M. G.; Kim, S.-G.; Park, G.-S.; Kawazoe, Y.; Lee, H. Moving Beyond Bimetallic-alloy to Single-atom Dimer Atomic-interface for All-pH Hydrogen Evolution. *Nat. Commun.* **2021**, *12*, 6766.

(34) Zhu, J.; Guo, Y.; Liu, F.; Xu, H.; Gong, L.; Shi, W.; Chen, D.; Wang, P.; Yang, Y.; Zhang, C.; Wu, J.; Luo, J.; Mu, S. Regulative Electronic States around Ruthenium/Ruthenium Disulphide Hetero-interfaces for Efficient Water Splitting in Acidic Media. *Angew. Chem., Int. Ed.* **2021**, *60*, 12328–12334.

(35) Liang, Q.; Zhong, L.; Du, C.; Luo, Y.; Zhao, J.; Zheng, Y.; Xu, J.; Ma, J.; Liu, C.; Li, S.; Yan, Q. Interfacing Epitaxial Dinickel Phosphide to 2D Nickel Thiophosphate Nanosheets for Boosting Electrocatalytic Water Splitting. *ACS Nano* **2019**, *13*, 7975–7984.

(36) Wang, Q.; Huang, X.; Zhao, Z. L.; Wang, M.; Xiang, B.; Li, J.; Feng, Z.; Xu, H.; Gu, M. Ultrahigh-Loading of Ir Single Atoms on NiO Matrix to Dramatically Enhance Oxygen Evolution Reaction. *J. Am. Chem. Soc.* **2020**, *142*, 7425–7433.

(37) Yu, H.; Xue, Y.; Huang, B.; Hui, L.; Zhang, C.; Fang, Y.; Liu, Y.; Zhao, Y.; Li, Y.; Liu, H.; Li, Y. Ultrathin Nanosheet of Graphdiyne-Supported Palladium Atom Catalyst for Efficient Hydrogen Production. *iScience* **2019**, *11*, 31–41.

(38) Zheng, X.; Cui, P.; Qian, Y.; Zhao, G.; Zheng, X.; Xu, X.; Cheng, Z.; Liu, Y.; Dou, S. X.; Sun, W. Multifunctional Active-Center-Transferable Platinum/Lithium Cobalt Oxide Heterostructured Electrocatalysts towards Superior Water Splitting. *Angew. Chem., Int. Ed.* **2020**, *59*, 14533–14540.

(39) Perdew, J. P.; Burke, K.; Ernzerhof, M. Generalized Gradient Approximation Made Simple. *Phys. Rev. Lett.* **1996**, *77*, 3865–3868.

(40) Kresse, G.; Furthmüller, J. Efficient Iterative Schemes for Ab Initio Total-Energy Calculations Using a Plane-Wave Basis Set. *Phys. Rev. B* **1996**, *54*, 11169–11186.

(41) Blöchl, P. E. Projector Augmented-Wave Method. *Phys. Rev. B* **1994**, *50*, 17953–17979.

(42) Kresse, G.; Joubert, D. From Ultrasoft Pseudopotentials to the Projector Augmented-Wave Method. *Phys. Rev. B* **1999**, *59*, 1758–1775.